# Viscous Flow Around a Propeller-Shaft Configuration with Infinite-Pitch Rectangular Blades

H. T. Kim* and F. Stern†
*Iowa Institute of Hydraulic Research,*
*University of Iowa, Iowa City, Iowa 52242*

**A viscous-solution method is set forth for calculating incompressible propeller flowfields. An overview of the computational method is given, and some example results for both laminar and turbulent flow are presented and discussed with regard to the flow physics for the idealized geometry of a propeller-shaft configuration with infinite-pitch rectangular blades. It is shown that the flow exhibits many of the distinctive features of interest, including the development and evolution of the shaft and blade boundary layers and wakes and tip, passage, and hub vortices. Comparisons are made with results from a lifting-surface, propeller-performance program to aid in evaluating the present method, which show that the method accurately predicts the blade loading, including viscous effects, and clearly displays the ability to resolve the viscous regions in distinction from the inviscid-flow approach.**

## Nomenclature

$A_\phi, B_\phi$, etc. = coefficients in transport equations
$a^i$ = contravariant base vector
$b_\ell^i$ = geometric tensor
$C_D, C_P, C_U, C_{nb}$ = finite-analytic coefficients ($nb = NE, NW, SE$, etc.)
$C_{F\theta}$ = force coefficient ($= 2F/\rho U_0^2 \pi R_p^2$)
$C_f$ = friction coefficient ($= 2\tau_w/\rho U_0^2$)
$C_\ell$ = section-lift coefficient ($= 2\ell/\rho U_0^2 c$)
$C_{Mx}$ = moment coefficient ($= 2M/\rho U_0^2 \pi R_p^3$)
$C_p$ = pressure coefficient
$c$ = blade chord length
$f_x, f_\theta, f_r$ = body force
$g^{ij}$ = conjugate metric tensor in general curvilinear coordinates $\xi^i$
$J$ = Jacobian
$k$ = turbulent kinetic energy
$L$ = characteristic (shaft) length
$p$ = pressure
$R$ = rotation parameter ($= \omega R_h / U_0$)
$Re, Re_c$ = Reynolds numbers ($= U_0 L/\nu$, $U_0 c/\nu$, respectively)
$R_h$ = hub radius
$R_p$ = propeller radius
$S_\phi, S$ = source functions
$t$ = time
$U, V, W$ = velocity components in cylindrical polar coordinates
$u, v, w$ = propeller-induced velocity
$U_c$ = wake centerline velocity
$U_0$ = characteristic (freestream) velocity
$U_\tau$ = wall-shear velocity [$= (\tau_w/\rho)^{1/2}$]
$\overline{uu}, \overline{vv}$, etc. = Reynolds stresses
$W_{\max}$ = maximum swirl velocity
$x, r, \theta$ = cylindrical polar coordinates
$x^+, y^+, z^+$ = dimensionless distances ($= U_\tau x/\nu$, etc.)
$\delta$ = boundary-layer thickness
$\epsilon$ = rate of turbulent energy dissipation
$\nu$ = kinematic viscosity
$\nu_t$ = eddy viscosity
$\xi, \eta, \zeta$ = body-fitted coordinates
$\tau$ = time increment
$\tau_w$ = wall-shear stress
$\phi$ = transport quantities ($U, V, W, k, \epsilon$)
$\Omega$ = angular velocity of rotating coordinates ($x, r, \theta$)
$\omega$ = propeller angular velocity

## Introduction

PROPELLER-TYPE flowfields are encountered in a wide variety of engineering problems, e.g., in the propulsion of marine vehicles, airplanes, and helicopters. The present study concerns the development of a viscous-solution method for the analysis of incompressible propeller flows. Of particular interest are marine propellers, which are unique because they operate in the thick stern boundary layer and near wake such that the flowfield is interactive; i.e., the propeller-induced flow is dependent on the hull flow, which is itself altered by the presence of the propeller. More specifically, here we are primarily concerned with the propeller-induced flow; however, the present study is an outgrowth of a large project concerning propeller-hull interaction and, upon extension, is expected ultimately to handle entire configurations.

Presently, only inviscid-flow methods are available for calculating practical marine-propeller flowfields.[1] Consistent with the restrictions of the underlying assumptions, the agreement with experimental thrust and torque data for nonuniform inflow has not been satisfactory. Also, the predicted pressure distributions, even for uniform inflow, do not show overall good agreement with experimental data. However, a complete evaluation of the theory has been hampered by the lack of knowledge of the effective inflow, which is usually assumed to be the nominal wake of the bare hull. Relatively little work has been done concerning viscous effects for rotating propeller blades. Most of the studies pertain to boundary-layer development and are restricted to laminar flow and idealized geometries.[2] Only one study has considered practical geometries and flow conditions.[3] In general, these methods

Received Sept. 4, 1989. 

*Graduate Research Assistant; currently Postdoctoral Associate.
†Associate Professor of Mechanical Engineering.

suffer due to the inaccuracy of the pressure distributions predicted by inviscid-flow methods and are not easily extendable into the wake.

Most work on propeller-hull interaction assumes that the interaction is inviscid in nature and has focused separately on either propeller influence on hull resistance (thrust deduction) or on hull boundary layer and wake (effective wake). Recently, Stern et al.[4,5] have developed a comprehensive viscous-flow approach to propeller-hull interaction in which a viscous-flow method for calculating ship stern flow[6] is coupled with a propeller-performance program in an interactive and iterative manner to predict the combined flowfield—hereafter referred to as the interactive approach. Following Schetz and associates (most recently, Ref. 7) and others, a body-force distribution is used to represent the propeller in the viscous-flow method. The steady-flow results show good agreement with experimental data and indicate that such an approach can accurately simulate the steady part of the combined propeller-hull flowfield. Although the unsteady-flow results generally follow the trends of available data, these results indicate the limitations of this approach for simulating the complex blade-to-blade flow. The work of Stern et al.[4,5] is precursory to the present work.

Most of the relevant work from related applications is for high-speed flows in which shock waves have a dominating influence; therefore, the focus of these studies is, in general, quite different from that of the marine-propeller application. The most closely related work is that done to develop energy efficient turboprops. Although advanced inviscid-flow[8] and viscous-flow[9] methods are under development, in most cases, incompressible-flow calculations are either not possible without major modifications or require the use of the pseudocompressibility concept. In its usual form, the latter precludes time-accurate unsteady-flow calculations, although some recent studies have shown promising results for such extensions through the use of subiterations. Lastly, concerning related applications, the helicopter-rotor,[10] turbomachinery,[11] and swirl-flow[12] calculations are helpful with regard to tip vortices, blade-to-blade flows, and swirling jets and wakes, respectively, but, here again, involve large differences in both flow conditions and geometry.

It is apparent from the foregoing that present methods for calculating incompressible propeller flowfields are inadequate for analyzing the detailed flow structures such as the development and evolution of the unsteady blade boundary layers and wakes, blade-to-blade flow, hub and tip vortices, and overall propeller wake. Furthermore, even the most advanced computational fluid dynamics methods from related applications are either inapplicable or require major modifications. This overall situation motivated the present study.

It is always desirable to choose as simple flow geometries as possible, both for calculations and experiments, without sacrificing the essential physics of the flow under consideration. The geometry chosen for this purpose is a propeller-shaft configuration with infinite-pitch rectangular blades (see Fig. 1). This geometry has the following important advantages: the grid generation is relatively simple so that the focus of attention can be given to the more basic aspects of the numerics; the laminar- and turbulent-flow solutions exhibit similar flow patterns such that meaningful comparisons can be made between the two flows; and the simplicity of the geometry facilitates the diagnosis of the important features of the blade-to-blade flow. Also, as will be shown later, the flowfield exhibits most of the distinctive features of interest. However, this geometry also has shortcomings, such as the lack of blade section geometry and, most importantly, thrust. Issues related to these aspects will be addressed in future extensions for practical geometries.

In the following, an overview of the computational method is provided. Then, some example results are presented and discussed with regard to the flow physics, including the computational grid and conditions and calculations for both laminar and turbulent flow. Subsequently, comparisons are made with results from a lifting-surface propeller-performance program to aid in evaluating the present method. Finally, some concluding remarks are made. The details of the computational method and the complete results, including additional calculations to study the influences of a thick-inlet boundary layer, the propeller angular velocity, and the blade number, as well as comparisons with some additional relevant experimental and computational studies, are provided by Kim.[13]

## Overview of the Computational Method

Consider the viscous flow around a propeller-shaft configuration rotating at constant angular velocity $\omega$ in an infinite uniform stream with velocity $U_0$ (Fig. 1). It is assumed that the Mach and cavitation numbers are, respectively, sufficiently small and large such that the fluid is incompressible and noncavitating. Under these conditions, the flow is cyclic in both space and time. Moreover, the flow is steady and spatially cyclic at blade-to-blade intervals in noninertial coordinates, which rotate with the propeller. As mentioned earlier, the present overall computational method is based on that used previously for calculating propeller-hull interaction.[4,5] This is expected to facilitate future extensions for entire configurations.

In order to extend this approach for the present purpose, a number of modifications were required, including the following: use of a noninertial coordinate system, which rotates with the propeller and solution of the corresponding equations; implementation of boundary conditions, including periodic boundary conditions for the blade-to-blade region; adoption of an alternating-direction implicit (ADI) scheme at each cross plane; and restructuring of the program for propeller geometries, including calculations for both laminar and turbulent flow. Also, during the time period that the present work was in progress, the basic viscous-flow method[6] was upgraded for fully elliptic calculations of the complete Reynolds-averaged Navier-Stokes equations.[14] Similar modifications were made for the present work. Lastly, modifications were required to execute the program efficiently on a supercomputer.

### Equations and Coordinate System

The Reynolds-averaged Navier-Stokes equations are written in the physical domain (see Fig. 2a) using noninertial cylindrical coordinates $(x,r,\theta)$ rotating with constant angular velocity $\Omega=(\omega,0,0)$ as follows:

$$\frac{\partial U}{\partial x}+\frac{\partial}{\partial r}(rV)+\frac{1}{r}\frac{\partial W}{\partial \theta}=0 \tag{1}$$

$$\frac{DU}{Dt}=-\frac{\partial}{\partial x}(p+\overline{uu})+f_x-\frac{\partial}{\partial r}(\overline{uv})$$
$$-\frac{1}{r}\frac{\partial}{\partial \theta}(\overline{uw})-\frac{uv}{r}+\frac{1}{Re}\nabla^2 U \tag{2}$$

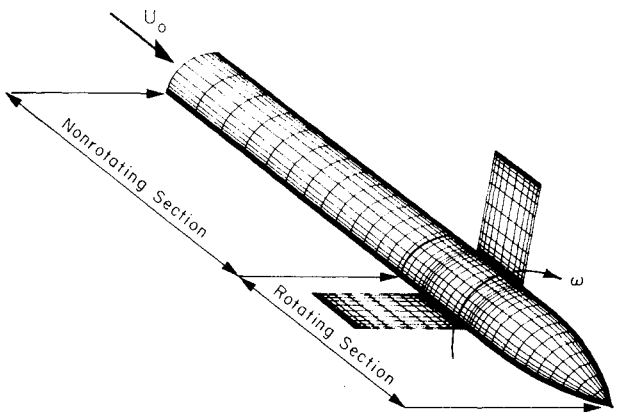


**Fig. 1 Propeller-shaft configuration with infinite-pitch rectangular blades.**

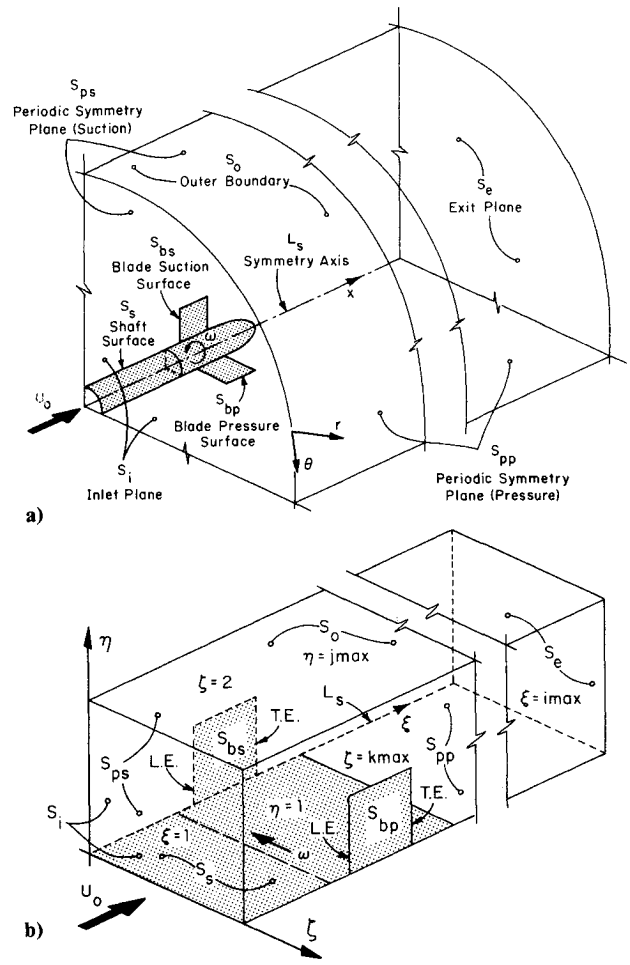


**Fig. 2 Solution domain: a) physical domain; b) computational domain.**

$$\frac{DV}{Dt} - \frac{W^2}{r} - 2\omega W - \omega^2 r = -\frac{\partial}{\partial x}(\overline{uv}) - \frac{\partial}{\partial r}(p + \overline{vv}) + f_r$$
$$-\frac{1}{r}\frac{\partial}{\partial \theta}(\overline{vw}) - \frac{1}{r}(\overline{vv} - \overline{ww}) + \frac{1}{Re}\left(\nabla^2 V - \frac{2}{r^2}\frac{\partial W}{\partial \theta} - \frac{V}{r^2}\right) \quad (3)$$

$$\frac{DW}{Dt} + \frac{VW}{r} + 2\omega V = -\frac{\partial}{\partial x}(\overline{uw}) - \frac{\partial}{\partial r}(\overline{vw})$$
$$-\frac{1}{r}\frac{\partial}{\partial \theta}(p + \overline{ww}) + f_\theta - \frac{2}{r}(\overline{vw})$$
$$+\frac{1}{Re}\left(\nabla^2 W + \frac{2}{r^2}\frac{\partial V}{\partial \theta} - \frac{W}{r^2}\right) \quad (4)$$

with

$$\frac{D}{Dt} = \frac{\partial}{\partial t} + U\frac{\partial}{\partial x} + V\frac{\partial}{\partial r} + \frac{W}{r}\frac{\partial}{\partial \theta}$$

and

$$\nabla^2 = \frac{\partial^2}{\partial x^2} + \frac{\partial^2}{\partial r^2} + \frac{1}{r}\frac{\partial}{\partial r} + \frac{1}{r^2}\frac{\partial^2}{\partial \theta^2}$$

where all variables have been nondimensionalized using $U_0$, $L$, and $\rho$. For laminar flow, Eqs. (1-4) reduce to the Navier-Stokes equations by simply deleting the Reynolds-stress terms and interpreting $(U,V,W)$ and $p$ as instantaneous values.

Closure of the Reynolds equations is attained through the use of the standard $k$-$\epsilon$ turbulence model. Each Reynolds stress is related to the corresponding mean rate of strain by the isotropic eddy viscosity $\nu_t$ as follows:

$$-\overline{uv} = \nu_t\left(\frac{\partial U}{\partial r} + \frac{\partial V}{\partial x}\right), \quad -\overline{uw} = \nu_t\left(\frac{1}{r}\frac{\partial U}{\partial \theta} + \frac{\partial W}{\partial x}\right)$$
$$-\overline{vw} = \nu_t\left(\frac{1}{r}\frac{\partial V}{\partial \theta} + \frac{\partial W}{\partial r} - \frac{W}{r}\right), \quad -\overline{uu} = \nu_t\left(2\frac{\partial U}{\partial x}\right) - \frac{2}{3}k$$
$$-\overline{vv} = \nu_t\left(2\frac{\partial V}{\partial r}\right) - \frac{2}{3}k, \quad -\overline{ww} = \nu_t\left(\frac{2}{r}\frac{\partial W}{\partial \theta} + 2\frac{V}{r}\right) - \frac{2}{3}k \quad (5)$$

$\nu_t$ is defined in terms of the turbulent kinetic energy $k$ and its rate of disspation $\epsilon$ by

$$\nu_t = C_\mu \frac{k^2}{\epsilon} \quad (6)$$

where $C_\mu$ is a model constant and $k$ and $\epsilon$ are governed by the modeled transport equations

$$\frac{Dk}{Dt} = \frac{\partial}{\partial x}\left(\frac{1}{R_k}\frac{\partial k}{\partial x}\right) + \frac{1}{r}\frac{\partial}{\partial r}\left(\frac{1}{R_k}r\frac{\partial k}{\partial r}\right)$$
$$+\frac{1}{r^2}\frac{\partial}{\partial \theta}\left(\frac{1}{R_k}\frac{\partial k}{\partial \theta}\right) + G - \epsilon \quad (7)$$

$$\frac{D\epsilon}{Dt} = \frac{\partial}{\partial x}\left(\frac{1}{R_\epsilon}\frac{\partial \epsilon}{\partial x}\right) + \frac{1}{r}\frac{\partial}{\partial r}\left(\frac{1}{R_\epsilon}r\frac{\epsilon}{\partial r}\right) + \frac{1}{r^2}\frac{\partial}{\partial \theta}\left(\frac{1}{R_\epsilon}\frac{\partial \epsilon}{\partial \theta}\right)$$
$$+ C_{\epsilon 1}\frac{\epsilon}{k}G - C_{\epsilon 2}\frac{\epsilon^2}{k} \quad (8)$$

$G$ is the turbulence generation term

$$G = \nu_t\left\{2\left[\left(\frac{\partial U}{\partial x}\right)^2 + \left(\frac{\partial V}{\partial r}\right)^2 + \left(\frac{1}{r}\frac{\partial W}{\partial \theta} + \frac{V}{r}\right)^2\right]\right.$$
$$+\left(\frac{\partial U}{\partial r} + \frac{\partial V}{\partial x}\right)^2 + \left(\frac{1}{r}\frac{\partial U}{\partial \theta} + \frac{\partial W}{\partial x}\right)^2$$
$$\left.+\left(\frac{1}{r}\frac{\partial V}{\partial \theta} + \frac{\partial W}{\partial r} - \frac{W}{r}\right)^2\right\} \quad (9)$$

The effective Reynolds number $R_\phi$ is defined as

$$\frac{1}{R_\phi} = \frac{1}{Re} + \frac{\nu_t}{\sigma_\phi} \quad (10)$$

in which $\phi = k$ for the $k$ equation [Eq. (7)] and $\phi = \epsilon$ for the $\epsilon$ equation [Eq. (8)]. The model constants are $C_\mu = 0.09$, $C_{\epsilon 1} = 1.44$, $C_{\epsilon 2} = 1.92$, $\sigma_U = \sigma_V = \sigma_W = \sigma_k = 1$, $\sigma_\epsilon = 1.3$.

The governing equations (1-10) are transformed into nonorthogonal curvilinear coordinates such that the computational domain (see Fig. 2b) forms a simple rectangular parallelepiped with equal grid spacing. The transformation is a partial one since it involves the coordinates only and not the velocity components $(U,V,W)$. The transformation is accomplished through the use of the expression for the divergence and "chain-rule" definitions of the gradient and Laplacian operators, which relate the orthogonal curvilinear coordinates $x^i = (x,r,\theta)$ to the nonorthogonal curvilinear coordinates $\xi^i = (\xi,\eta,\zeta)$. In this manner, the governing Eqs. (1-10) can be rewritten in the following form of the continuity and convective-transport equations:

$$\frac{\partial}{\partial \xi}\left(b_1^1 U + b_2^1 V + b_3^1 W\right) + \frac{\partial}{\partial \eta}\left(b_1^2 U + b_2^2 V + b_3^2 W\right)$$
$$+\frac{\partial}{\partial \zeta}\left(b_1^3 U + b_2^3 V + b_3^3 W\right) = 0 \quad (11)$$

$$g^{11}\frac{\partial^2\phi}{\partial\xi^2}+g^{22}\frac{\partial^2\phi}{\partial\eta^2}+g^{33}\frac{\partial^2\phi}{\partial\zeta^2}=2A_\phi\frac{\partial\phi}{\partial\zeta}+2B_\phi\frac{\partial\phi}{\partial\eta}+2C_\phi\frac{\partial\phi}{\partial\xi}+R_\phi\frac{\partial\phi}{\partial t}+S_\phi \tag{12}$$

#### Discretization and Velocity-Pressure Coupling

The convective-transport equation (12) is reduced to algebraic form through the use of a revised and simplified version of the finite-analytic method.[14] In this method, Eq. (12) is linearized in each local rectangular numerical element $\Delta\xi=\Delta\eta=\Delta\zeta=1$ by evaluating the coefficients and source functions at the interior node $P$ and transformed again into a normalized form by a simple coordinate stretching. An analytic solution is derived by decomposing the normalized equation into one- and two-dimensional partial-differential equations. The solution to the former is readily obtained. The solution to the latter is obtained by the method of separation of variables with specified boundary functions. As a result, a 12-point, finite-analytic formula for unsteady, three-dimensional, elliptic equations is obtained in the form

$$\phi_P=\frac{1}{1+C_P\left(C_U+C_D+\frac{R}{\tau}\right)}\left[\sum_1^8 C_{nb}\phi_{nb}+C_P\left(C_U\phi_U+C_D\phi_D+\frac{R}{\tau}\phi_P^{n-1}\right)-S\right] \tag{13}$$

It is seen that $\phi_P$ depends on all eight neighboring nodal values in the crossplane, the values at the upstream and downstream nodes $\phi_U$ and $\phi_D$, and the values at the previous time step $\phi_P^{n-1}$. For large values of the cell Reynolds number, Eq. (13) reduces to the partially parabolic formulation used previously.[4,5] Since Eq. (13) is implicit, both in space and time, at the current crossplane of calculation, its assembly for all elements results in a set of simultaneous algebraic equations. If the pressure field is known, this equation can be solved by the method of lines. However, since the pressure field is unknown, it must be determined such that the continuity equation is also satisfied.

The coupling of the velocity and pressure fields is accomplished through the use of a two-step, iterative procedure involving the continuity equation based on the SIMPLER algorithm. In the first step, the solution to the momentum equations for a guessed pressure field is corrected at each crossplane such that continuity is satisfied. However, in general, the corrected velocities are no longer a consistent solution to the momentum equations for the guessed $p$. Thus, the pressure field must also be corrected. In the second step, the pressure field is updated again through the use of the continuity equation. This is done after a complete solution to the velocity field has been obtained for all crossplanes. Repeated global iterations are thus required in order to obtain a converged solution. The procedure is facilitated through the use of a staggered grid. Both the pressure correction and pressure equations are derived in a similar manner by substituting Eq. (13) for $(U,V,W)$ into the discretized form of the continuity equation [Eq. (11)] and representing the pressure-gradient terms by finite differences.

#### Solution Domain and Boundary Conditions

The physical and computational solution domains are shown in Figs. 2. The boundary conditions on each of the boundaries are as follows: on the inlet plane $S_i$, the initial conditions for $\phi$ are specified from simple flat-plate solutions; on the shaft $S_s$ and blade surfaces $S_{bs}$ and $S_{bp}$ for laminar flow, the solution is carried out up to the actual surface where the no-slip condition is applied; for turbulent flow, a two-point, wall-function approach is used; on the exit plane $S_e$, axial diffusion is negligible so that the exit conditions used are $\partial^2\phi/\partial\xi^2=0$, and a zero-gradient condition is used for $p$; on the periodic symmetry planes $S_{ps}$ and $S_{pp}$, an explicit periodicity condition is imposed, i.e., $\phi(\xi,\eta,\zeta)=\phi(\xi,\eta,\zeta+\zeta_p)$, $p(\xi,\eta,\zeta)=p(\xi,\eta,\zeta+\zeta_p)$, where $\zeta_p$ corresponds to the blade-to-blade interval; on the symmetry axis $L_s$, the conditions imposed are $V=W=0$, $\partial(U,k,\epsilon,p)/\partial\eta=0$; and on the outer boundary $S_0$, the uniform-flow condition is applied, i.e., $U=1$, $W=\omega r|_{S_0}$, $p=\partial(k,\epsilon)/\partial\eta=0$.

## Results

In the following, the computational grid and conditions are described first. Then, some example results for laminar flow are discussed to point out the essential features of the solutions. These are followed by a brief presentation of the results for turbulent flow to highlight the differences. This order and emphasis of discussion is selected since the former represent solutions to the exact governing equations, whereas the latter are dependent on the choice of turbulence model.

#### Computational Grids and Conditions

The computational grid is obtained using the technique of generating body-fitted coordinates through the solution of elliptic partial differential equations. Because of the simplicity of the present propeller geometry (see Fig. 1), it is possible to specify the transverse and longitudinal sections of the computational domain as surfaces of constant $\xi$ and $\zeta$, respectively, and moreover, the three-dimensional grid is obtained by simply rotating the two-dimensional grid for the longitudinal plane. The present geometry of the propeller-shaft configuration was specified based on a configuration for which calculations had been previously performed,[5] i.e., P4660. However, the actual propeller for P4660 was replaced by one with an equivalent blade area ratio, but, as already indicated, with infinite-pitch rectangular (i.e., flat-plate) blades.

Partial views of the grid used in the calculations are shown in Figs. 3a and 3b for a longitudinal plane and a typical body crossplane, respectively. The shaft and blade surface grid is shown in Fig. 1. Similar grids are used for both the laminar and turbulent calculations, but, in the latter case, the near-wall grid lines ($y^+<30$) are deleted in order to implement the two-point, wall-function approach. The inlet, exit, and outer boundaries are located at $x=(0.54,6)$ and $r=0.9$, respectively; for laminar flow, the first grid points off the body and blade surfaces are located at $0.4<y^+<8$ and $1<x^+,y^+$, or $z^+<14$, respectively; for turbulent flow, the first grid points off the body and blade surfaces are located at $30<y^+<230$ and $40<x^+$, $y^+$, or $z^+<190$, respectively; 62 axial grid points were used, with 18 over the upstream portion of the shaft up to the blade leading edge, 11 over the blade, 14 over the remainder of the shaft from the blade trailing edge to the hub apex, and 19 over the wake; for laminar flow, 40 radial grid points were used with 22 over the blade span and 18 from the tip to the outer boundary; for turbulent flow, 36 radial grid points were used with 19 over the blade span and 17 from the tip to the outer boundary; 30 and 26 angular grid points were used for laminar and turbulent flow, respectively. In summary, the total number of grid points for the laminar and turbulent calculations are 74,400 and 58,032, respectively.

The conditions for the calculations are as follows: $L=1$; $U_0=1$; for laminar flow, $Re=2.02\times10^6$ and $Re_c=1\times10^5$; for turbulent flow, $Re=6.08\times10^6$ and $Re_c=3\times10^5$; the propeller angular velocity $\omega=0.3\pi$ (=9 rpm) (the blade section angle of attack varies from 1.2 deg at the root to 4 deg at the tip); for laminar flow, on the inlet plane, $\delta/R_h=0.111$ and there is no inviscid-flow overshoot; and for turbulent flow, on the inlet plane, $\delta/R_h=0.489$, $U_\tau=0.04$, and the inviscid-flow overshoot is 1.01. The $\delta$ values are based on simple flat-plate solutions and the selected $Re$. For laminar flow, the $Re$ value was selected based on the fact that many investigators have performed two-dimensional, flat-plate boundary-layer and wake

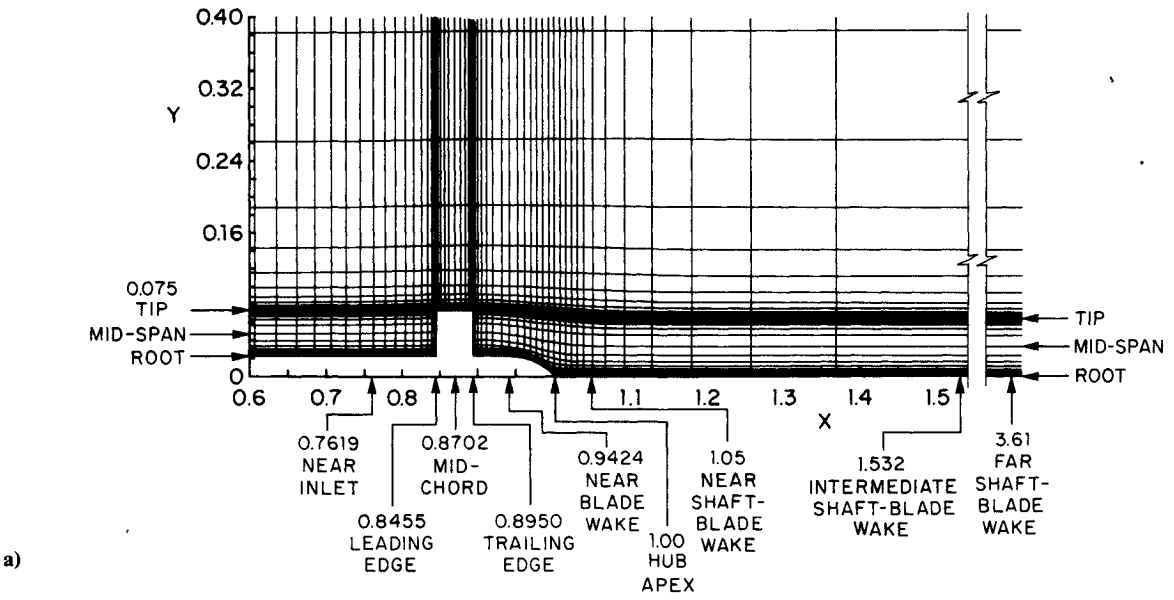


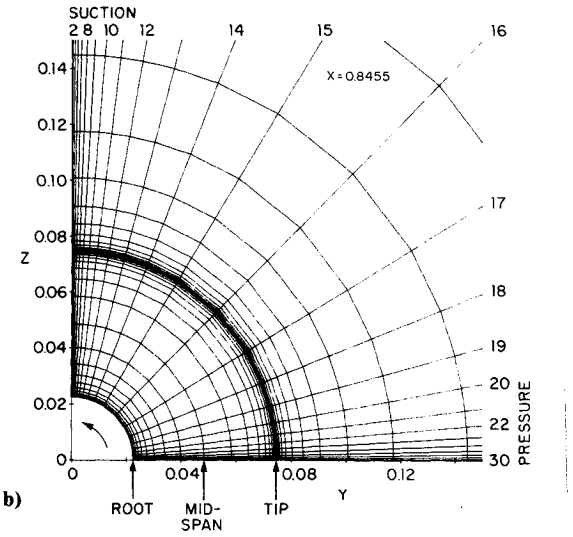


**Fig. 3 Computational grid: a) longitudinal plane. b) body cross-plane.**

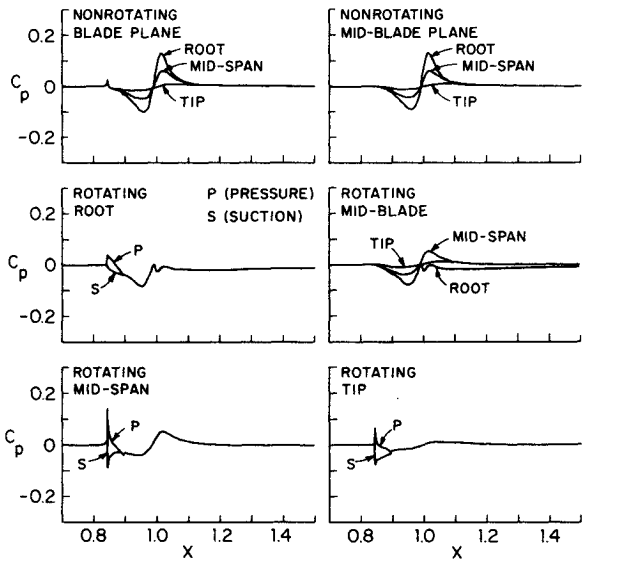


**Fig. 4 Shaft and blade surfaces and wake pressure: laminar flow.**

calculations for this same value. For turbulent flow, a reasonable value of $Re$ was selected for which fully turbulent flow over the shaft and blades is probable. The propeller angular velocity was taken to be sufficiently low such that no separation occurs over the blades.

For the nonrotating condition, the calculations were begun with a zero-pressure initial condition for the pressure field. For the rotating condition, the complete nonrotating solution was used as the initial condition. The values of the time $\alpha_t$ and pressure $\alpha_p$ under-relaxation factors and total number of global iterations used in obtaining the solutions are 0.02–0.1, 0.03–0.1, and 70–100, respectively. The calculations were performed on a CRAY X-MP/48 supercomputer. The central processor unit (CPU) and storage (words) that were required for each of the solutions are about 30 min and 1–1.7 M words, respectively. Note that the computer codes were 23% vectorized and optimized to achieve a 65% reduction in CPU and that the maximum normal system storage limit is 2 M words.

### Laminar Flow

The laminar-flow results for both the nonrotating and rotating conditions are shown in Figs. 4–11. Figures 4, 5, and 6 show the variation of some properties in the longitudinal direction, i.e., the shaft and blade surfaces and wake pressure, the wall-shear (magnitude and angle for inertial coordinates), and the wake centerline and maximum swirl velocities, respectively. Figures 7–10 show the detailed results for some representative axial stations in the form of velocity and pressure profiles (i.e., $\phi$ vs $Y=r/R_p$), axial-velocity contours, cross-plane-velocity vectors (noninertial coordinates for the blade region and inertial coordinates for the blade wake region), and axial-vorticity $\omega_x$ contours, respectively. Last, Fig. 11 shows closeup views of the tip vortex. Note that, in Fig. 7, the ordinate is $Y$ such that the distance from the blade surface is larger near the tip than near the root, and the labeling of each of the curves corresponds to the angular grid lines shown in Fig. 3b. Also, the discussion to follow is based on the complete results, which include solution profiles and contour and vector plots at all of the stations designated in Fig. 3a; however, for brevity of presentation, only representative stations are displayed in Figs. 7–10 for the rotating condition.

First, consideration is given to the results for the nonrotating condition. The shaft and blade surfaces and wake pressure variations (see Fig. 4) for the midblade plane (plane through grid line 16 of Fig. 3b) indicate a minimal influence of the blades and are typical of trailing-edge flow in the presence of a thin boundary layer; however, at this relatively low $Re$ (laminar flow), the adverse axial-pressure gradient associated with

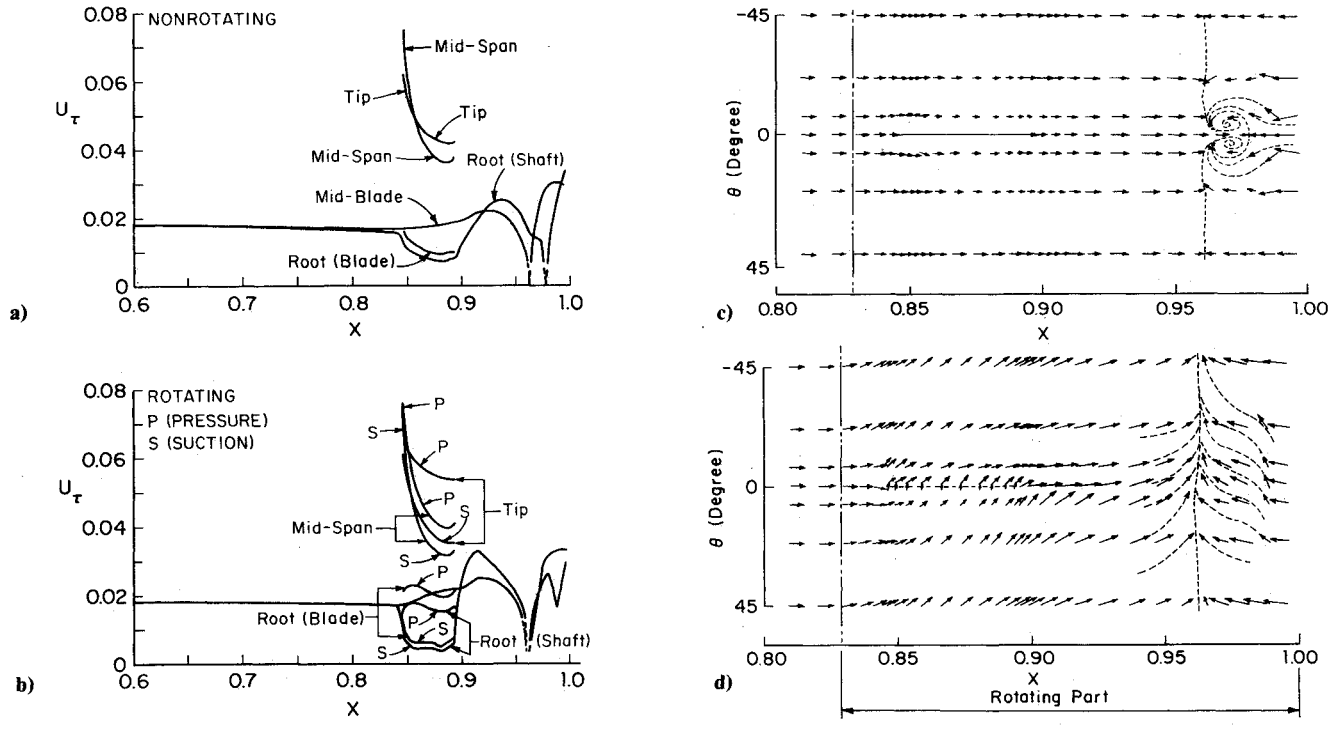


**Fig. 5 Wall-shear velocity: laminar flow: a) magnitude: nonrotating; b) magnitude: rotating; c) vector: nonrotating; d) vector: rotating.**

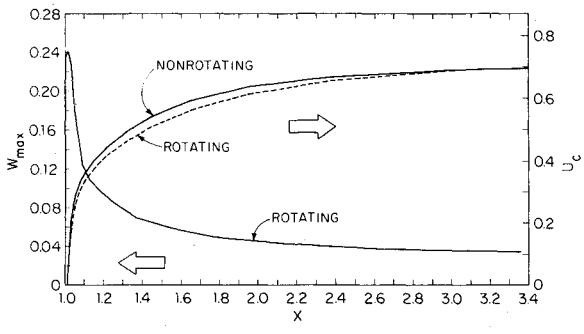


**Fig. 6 Wake centerline and maximum swirl velocities: laminar flow.**

the closing of the body is sufficient to cause a small separation region in the vicinity of the hub apex, $0.96 < x < 1.01$. Note the rapid rate of recovery of pressure in the radial direction. The pressure variations for the blade plane (planes through grid lines 2 and 10 of Fig. 3b) are similar, but clearly show the effects of the blade leading and trailing edges as well as a small displacement effect of the blade boundary layer.

The $U_\tau$ variations (see Fig. 5a) are consistent with those just described for the pressure. Note that $U_\tau$ ($=\sqrt{C_f/2}$) has been used instead of $C_f$ to facilitate the comparisons with the turbulent-flow results. For the blade plane, there is a large reduction of $U_\tau$ in the juncture region due to the flow retardation and also in conjunction with the relatively large boundary-layer thickness there and a downstream shift of the region of low $U_\tau$ associated with the flow separation as compared to the midblade plane. The latter is consistent with the differences in separation patterns for the blade and midblade planes. On the blade, initially $U_\tau$ is larger at the midspan than at the tip in response to the larger leading-edge pressure peak at midspan, then the trend reverses. The wall-shear velocity vector (Fig. 5c) is generally aligned with the axial direction except near the blade leading edge where the blade displacement effects are evident and in the separation region where the complex topological nature of the three-dimensional separation is displayed.

The wake centerline velocity $U_c$ (see Fig. 6) displays the extent of the separation region and the recovery of the wake. The $W_{max}$ is, of course, nearly zero for the nonrotating condition and not shown. The asymptotic forms display the details of the recovery of the wake. Although the exit plane is 34 diam downstream of the propeller plane (equivalently 5 shaft lengths downstream of the hub apex), the slope of the velocity defect of the shaft wake has not yet reached its asymptotic value. In contrast, the slope of the blade wake velocity defect is close to the asymptotic value. The exit plane is 103 chord lengths downstream from the blade trailing edge.

Last, for the nonrotating condition, the detailed results are discussed. At the near-inlet station, the solution displays the characteristics of the inlet conditions, i.e., an axisymmetric, thin, laminar boundary layer. At the leading-edge and midchord stations, the solution shows the initiation of the blade boundary layer, including leading-edge (stagnation-point) and displacement effects. Also, the juncture flow indicates a weak leading-edge horseshoe vortex. At the trailing-edge station, the trailing-edge effects of both the blade and the shaft are predominate, including a reversal of the juncture flow. At the near-blade wake station and hub apex, the solution shows the initial development of the blade wake. Here again, the effects of the shaft trailing edge are quite large. Two corner vortices are apparent near the shaft axis, which are an indication of the nature of the flow within the separation region. At the near, intermediate, and far shaft-blade wake stations, the solution shows the recovery of shaft and blade wakes. The crossplane flow and pressure recover more rapidly than the axial velocity component.

Next, consideration is given to the results for the rotating condition. Referring to Fig. 4, in the vicinity of the hub apex and in the near wake, there is a decrease in pressure due to the propeller-induced swirl. The lifting effects due to the angle of attack of the blade section are clearly evident. Note that the pressure peak is at the blade leading edge such that just upstream of the leading edge very large adverse and favorable pressure gradients occur for the pressure and suction sides of the blade, respectively, whereas just downstream of the leading edge the reverse holds true.

The wall-shear velocity $U_\tau$ (see Fig. 5b) shows slightly increased values over the spinning portion of the shaft and greater uniformity between the blade and midblade planes in

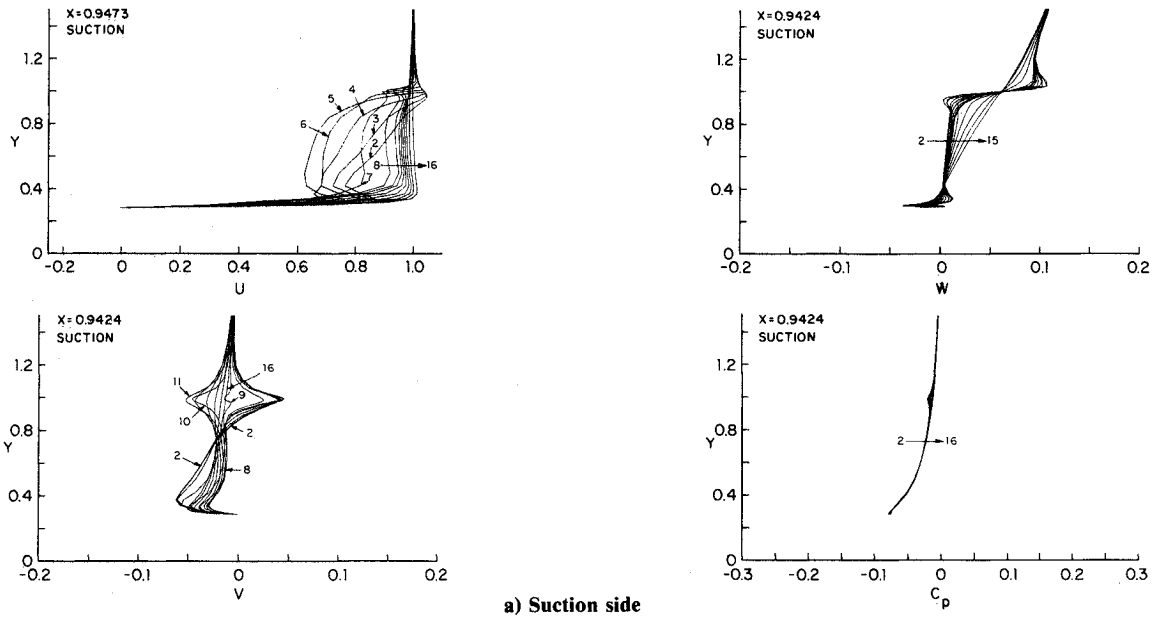


a) Suction side

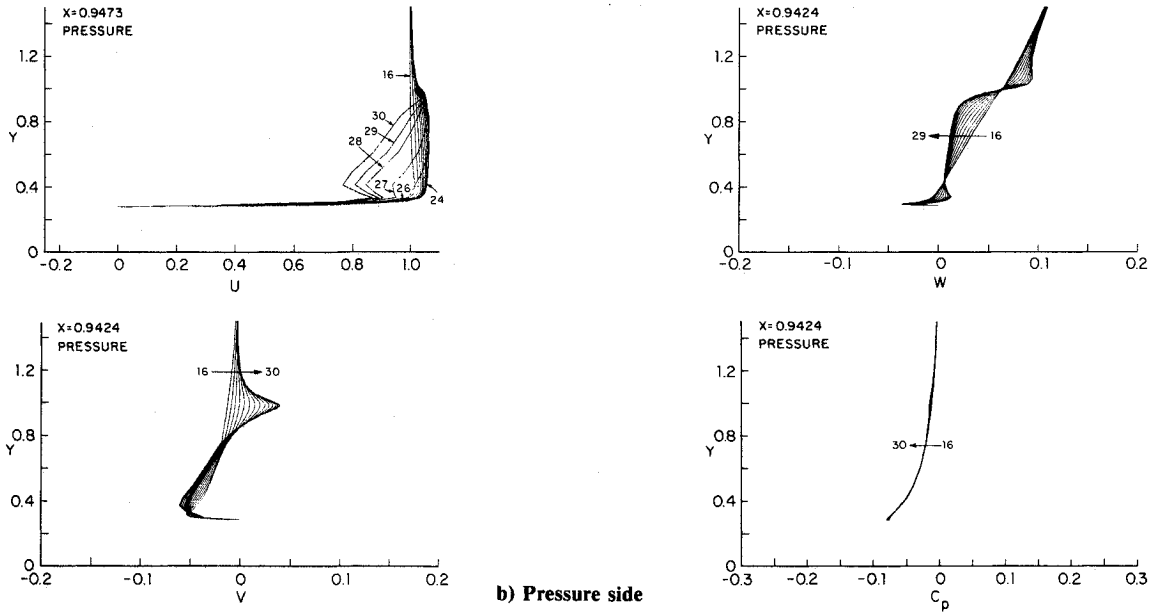


b) Pressure side

Fig. 7 Velocity and pressure profiles; laminar flow, rotating.

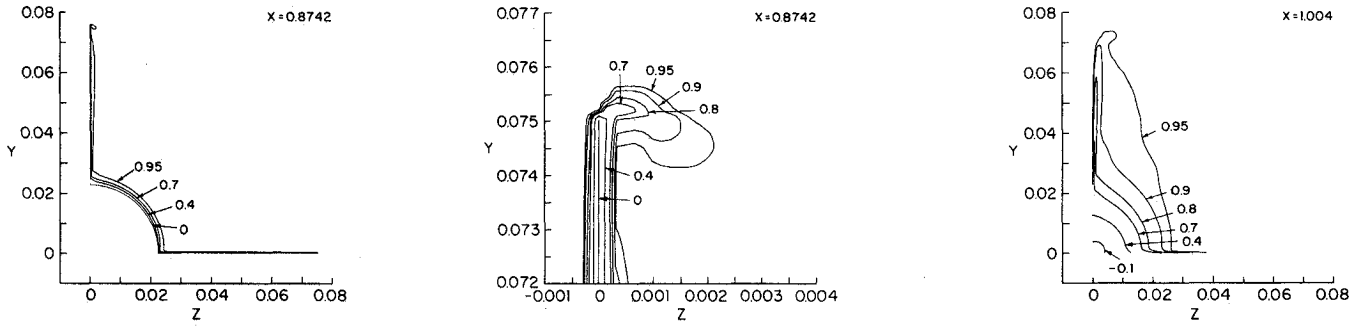


Fig. 8 Axial-velocity contours: laminar flow, rotating.

the separation region as compared to the nonrotating condition. For the present conditions, the rotation parameter $R$ is quite small, i.e., $R = 0.02$, which explains the only slight increase in $U_\tau$ as compared to the previous calculations.[5] On the blades, $U_\tau$ is smaller on the suction than on the pressure side, in conjunction with the relatively thicker boundary layer on the suction as compared to the pressure side. Consistent with the results for the nonrotating condition, $U_\tau$ is larger at the tip than at midspan except near the leading edge. On the rotating section, the wall-shear velocity vector (see Fig. 5d) shows large effects due to rotation, i.e., the flow is turned toward the direction of rotation. In the blade region, the passage vortex is evident, including its helical nature. In the separation region, the flow is completely turned in the direction of rotation,

which results in the aforementioned greater uniformity in the separation patterns between the blade and midblade planes. Over the blade, the wall-shear velocity vector is in the axial direction, except near the tip, where the flow is outward, especially on the pressure side.

Figure 6 shows that the recovery of $U_c$ is slower for the rotating than the nonrotating condition. This is due to the adverse axial-pressure gradient induced by the hub vortex. Also shown is the decay of $W_{max}$ in the wake, which is associated with the intensity and decay rate of the hub vortex. Finally, the asymptotic forms indicate that the shaft wake is unaffected, the blade-wake slope is increased, and the swirl decay is relatively faster than that of the axial-velocity defect.

The detailed results vividly display the complexity of the flow for the rotating condition. At the leading edge, the solution shows the initiation of the blade boundary layer, in this case, with significant differences between the suction and pressure sides of the blade due to the influences of the aforementioned abrupt changes in the pressure gradients. Interestingly, the boundary layers on both sides of the blade are thicker for the rotating than the nonrotating condition. The tip-vortex formation initiates with flow around the tip from the pressure to the suction side. The vortical flow is asymmetric such that the tangential velocity component is larger on the suction than the pressure side, whereas the situation is reversed for the radial velocity component. The passage-vortex formation also initiates and dominates the juncture flow. At the midchord station and trailing edge, the effects of the pressure gradient changes are clearly displayed; i.e., on the suction and pressure sides, the flow is decelerated and accelerated, respectively. On the suction side, the boundary-layer thickness varies considerably across the span. The tip vortex has lifted off the suction-side surface such that the radial velocity component is positive on both sides. Braiding of the fluid from both the suction and pressure sides is apparent, but particle trajectories were not traced to display this phenomenon. The pressure is surprisingly uniform in view of the crossplane flow; however, very low values are observed in the tip-vortex core. The passage vortex increases in size, and its core moves toward the suction side. The axial-velocity and axial-vorticity contours are hook shaped near the tip due to the influences of the tip vortex. At the near blade wake station and hub apex, the solution shows the development of the blade wakes, which indicate the characteristics of the complex mixing of the suction and pressure side three-dimensional boundary layers, including significant effects of the tip, passage, and hub vortices and the hub-induced pressure gradients. The minimum velocity in the wake migrates toward the suction side. There is a rapid recovery of the pressure-side wake such that the velocity-defect region is mainly behind the shaft and off the suction side of the blade. The blade wake becomes quite thick as it merges with the wake of the shaft and the tip vortex. There is a region of backward flow near the wake axis associated with the flow separation. The tip vortex reduces in intensity, and the passage vortex

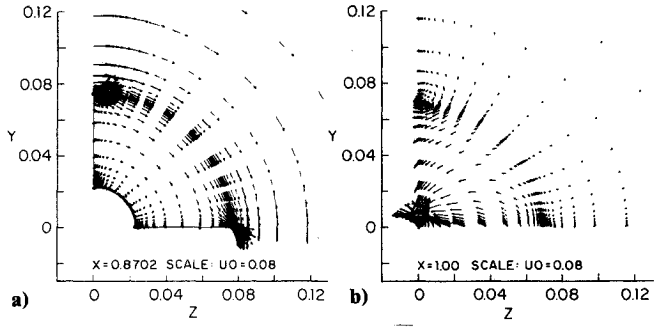


Fig. 9 Crossplane-velocity vectors: laminar flow, rotating.

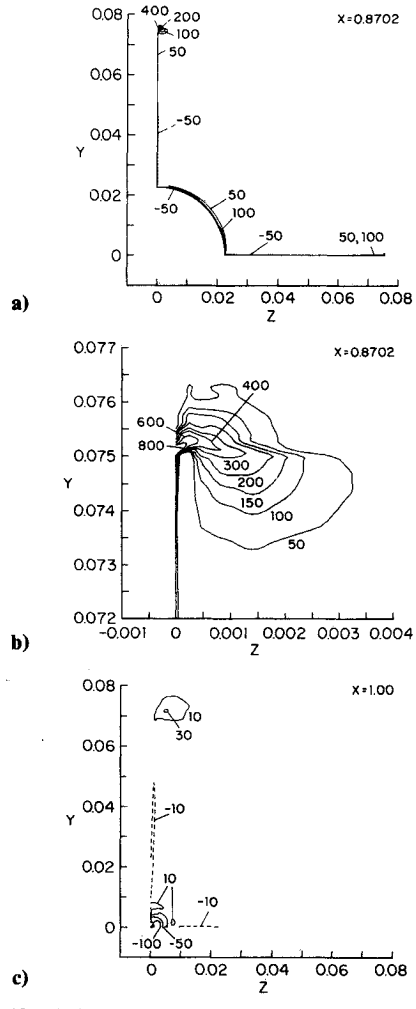


Fig. 10 Axial-vorticity contours: laminar flow, rotating.

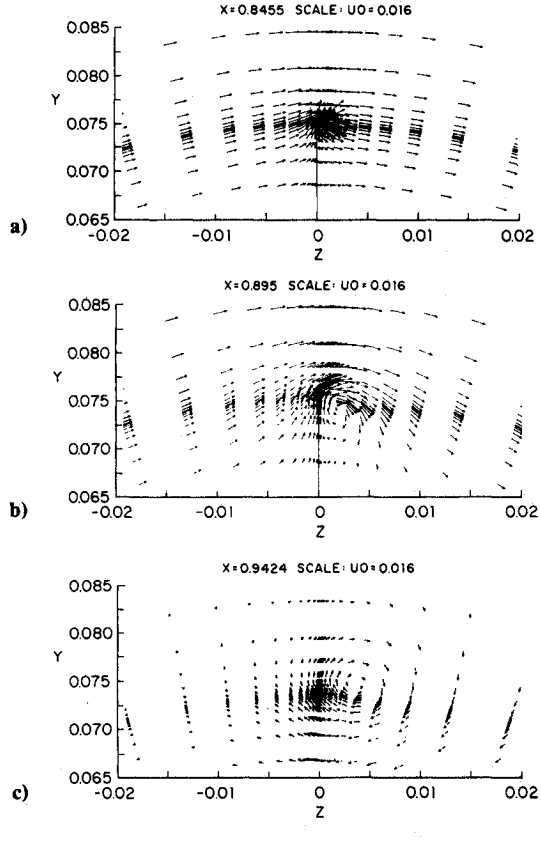


Fig. 11 Closeup view of the tip vortex: laminar flow, rotating.

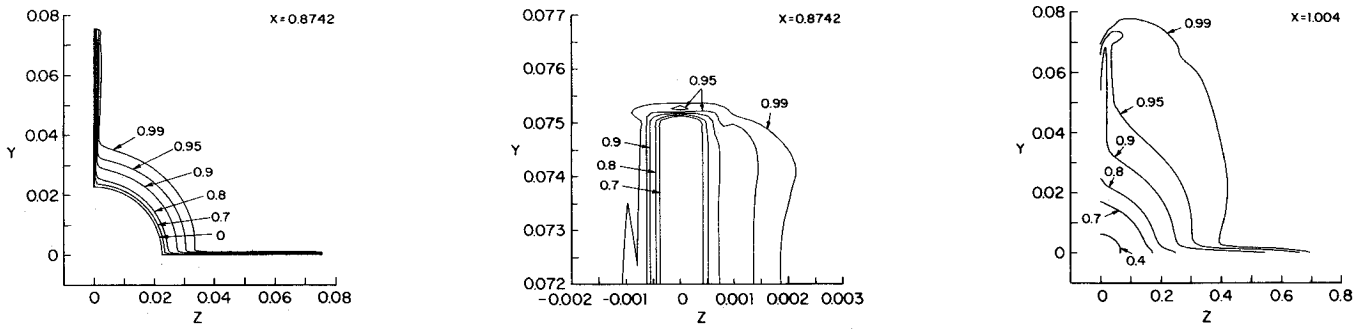


Fig. 12 Axial-velocity contours: turbulent flow, rotating.

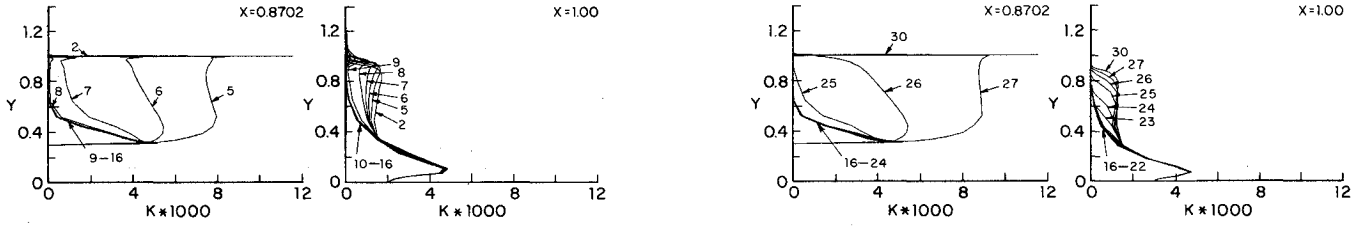


a) Suction side b) Pressure side

Fig. 13 Turbulent kinetic energy profiles: rotating.

merges into a large asymmetric hub vortex. Finally, at the near, intermediate, and far shaft-blade wake stations, the nature of the recovery of the wake is displayed. It is clear that the circumferential mixing is faster for the rotating than the nonrotating condition.

The closeup views of the tip vortex shown in Fig. 11 clearly display its initiation at the blade leading edge, subsequent migration off the surface along the blade chord, and decay as it is convected and diffuses into the wake. Also, the views reveal the mechanism of the tip-vortex formation. At the leading edge, nearly all of the fluid forming the tip vortex originates from the pressure side, whereas further downstream the suction side fluid is "pumped" into the tip vortex. This indicates a "braiding" process, which is often referred to as the tip-vortex rollup. It should be mentioned that a part of the diffusion of the tip vortex may be numerical due to the large grid expansion from the blade to the midblade planes.

#### Turbulent Flow

Some limited turbulent-flow results are shown in Figs. 12 and 13. The turbulent-flow results are consistent with and very similar to those for laminar flow. In general, the differences are as expected based on physical reasoning; i.e., viscous effects are confined to narrower regions and the three dimensionality of the flow is considerably reduced for turbulent as compared to laminar flow. Also, quite apparent for turbulent flow is the reduced resolution near solid surfaces and the wake centerplane due to the present wall-function approach.

The overall trends described earlier with regard to the shaft and blade surfaces and wake pressure, wall-shear velocity, and wake centerline and minimum swirl velocities are quite similar; however, the pressure peak at the hub apex is considerably larger, and there are some differences in the wall-shear velocity behavior due to the absence of separation. The detailed results are also quite similar. However, for the nonrotating condition, the juncture effects are minimal, and the crossplane flow and pressure variations are reduced, whereas, for the rotating condition, the tip and passage vortices are larger and persist longer, the latter merges into a larger hub vortex, lower pressures are observed in the tip-vortex core, and the recovery of the wake is considerably faster. The turbulent kinetic-energy profiles show two peaks, one near the wake centerline and one corresponding to the tips of the blades.

## Comparison with Results from a Lifting-Surface Propeller-Performance Program

Unfortunately, no experimental information is available for the present geometry. Therefore, to aid in evaluating the present work, comparisons have been made with some relevant experimental and computational studies, including the following topics: juncture flow, which is related to the present flow in the blade-hub juncture region for the nonrotating condition; tip flow, which is related to the present flow in the tip region for the rotating condition; turbomachinery flow, which is related to the present blade boundary-layer and wake development and blade-to-blade flow; and propeller flow, which is, of course, the topic and goal of the present study. Although in most cases the comparisons are only qualitative due to the large differences between the topic and present geometries, they support the present results in that the predicted flow structures are similar and consistent with the results from these studies. The complete comparisons are lengthy and beyond the scope of the present paper (see Kim[13]). Herein, only the direct comparisons between the present turbulent-flow results and those from a lifting-surface propeller-performance program[15] will be presented.

Figures 14 show a comparison of the chordwise and spanwise distributions of the blade loading in terms of the pressure jump (see Fig. 14a) and section-lift coefficient (see Fig. 14b). A large difference in the pressure jump is observed near the leading edge. Differences are also seen in the section-lift coefficient. The viscous results show considerably larger values near the root and the tip but smaller values for the midspan region. The higher root loading for the viscous flow is, no doubt, a result of the increased effective angle of attack due to the oncoming shaft boundary layer. However, a part of the diference may be due to the lack of hub effects in the lifting-surface, propeller-performance program. The lower midspan loading is consistent with the aforementioned differences in chordwise loading near the leading edge. The higher tip loading may be due to the reduced pressure on the suction side due to the tip vortex. Interestingly, in spite of these differences in the loading distributions, the total forces and moments show remarkably close agreement.

Figures 14c and 14d show a comparison of the propeller-induced velocities $(u,v,w)$ just upstream and downstream of the

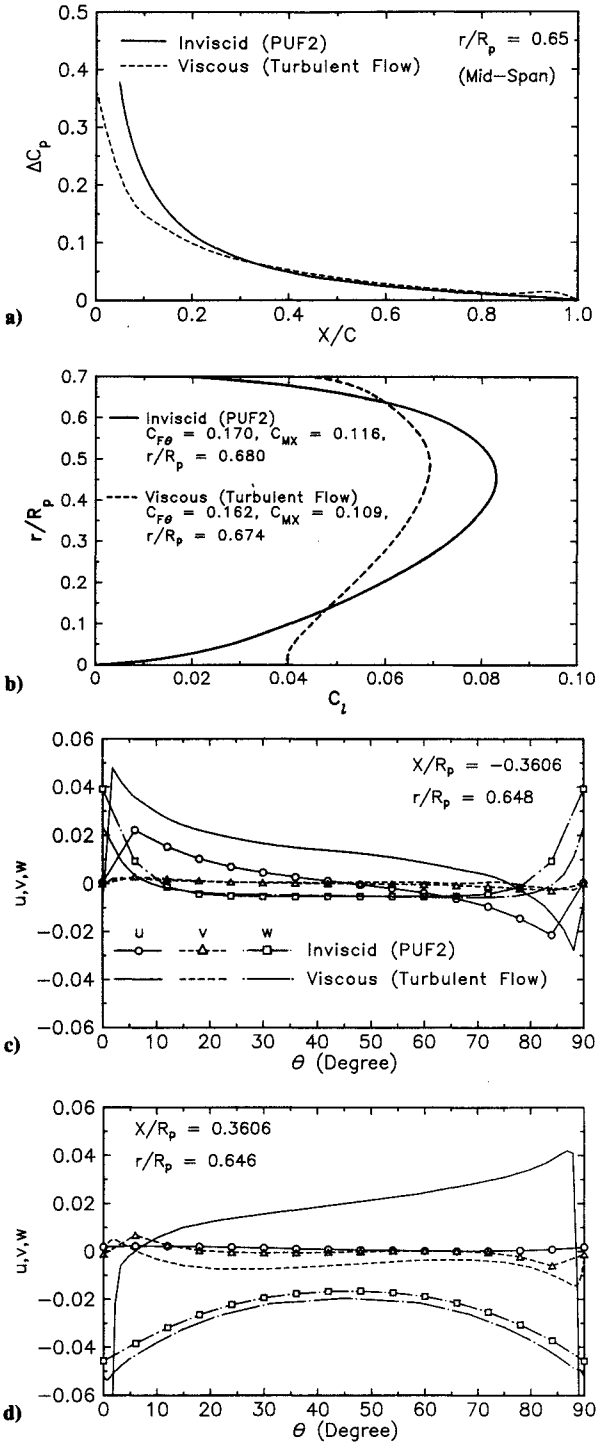


**Fig. 14 Comparison of turbulent-flow and lifting-surface propeller-performance program results: a) chordwise loading; b) spanwise loading; c) upstream propeller-induced velocity; d) downstream propeller-induced velocity.**

propeller at the midspan radius. For the viscous-flow solution, $(u,v,w)$ is defined as the total velocity, $(U,V,W)$ minus the freestream $(U_0,0,0)$ value. Results are shown using the blade angle coordinate $\theta = \omega t$ as the abscissa for the entire blade-to-blade region from the suction ($\theta = 0$ deg) to the pressure side ($\theta = 90$ deg).

The velocity components just upstream of the propeller (see Fig. 14c) clearly show the effects of the leading-edge stagnation point. The $u$ velocity components show similar trends; i.e., the point of the minimum velocity shifts to the pressure side, which suggests that the stagnation point also shifts to the pressure side. The increased magnitude for the viscous solution may be due to the prescribed overshoot for the oncoming shaft boundary layer. The $v$ velocity component is nearly zero for both results. The $w$ velocity components also show similar trends; however, the inviscid solution indicates a stronger local effect of the leading-edge stagnation point than the viscous solution such that the circumferential average is zero for the inviscid but not the viscous solution; i.e., the viscous solution indicates small negative preswirl.

The velocity components just downstream of the propeller (see Fig. 14d) highlight the differences between the viscous and inviscid solutions. The inviscid $u$ velocity component shows very small positive values from the suction to the pressure side, whereas the viscous $u$ velocity component shows a large change from the suction to the pressure side; i.e., the viscous blade wake appears as a sharp drop on both the suction and pressure sides and the effects of the retarded suction-side and accelerated pressure-side boundary layers are clearly evident. The $v$ velocity components show similar trends but with somewhat larger variations for the viscous solution. The $w$ velocity components also show similar trends, but with larger swirl for the viscous solution in spite of the smaller loading.

## Concluding Remarks

The present work was motivated by the limitations of the interactive approach for simulating the complex blade-to-blade flow. This has certainly been accomplished by the present viscous-solution method, albeit for an idealized geometry. In fact, the present work provides, for the first time, a very detailed documentation of the viscous flow around a propeller for both laminar and turbulent flow. It is concluded that the present approach is capable of simulating incompressible propeller flowfields, including both the propeller loading and the complex blade-to-blade flow, and should be extended for practical geometries. It is also concluded, based on the comparison of the laminar and turbulent results, that, although most aspects of the flow are governed by pressure-gradient effects, improvements in turbulence-modeling procedures, especially near-wall treatment, are important to resolve certain flow features, including transition, separation, and small-scale vortical structures such as leading-edge horseshoe and secondary vortices.

Of course, much more work needs to be done to extend the method to realistic propeller and body geometries. Some of the issues that need to be addressed are optimum coordinates, including investigations of inertial and helical systems, and optimum grid-generation techniques for complex, three-dimensional, propeller-driven bodies, including investigations of domain decomposition methods with moving and adaptive grids. As already mentioned, improved turbulence-modeling procedures are essential and possibly, as often stated, a pacesetting issue. Also, further development of solution algorithms is a necessity in order to perform the required large-scale computations even on the most advanced, available supercomputers. It should be recognized that none of these issues is trivial; on the contrary, all require substantial effort so that it is expected that the present problem will remain a challenge for many years to come.

## Acknowledgments

This research was initially sponsored by the Office of Naval Research, Accelerated Research Initiative Program in Propulsor-Body Hydrodynamic Interactions under Contract N00014-85-K-0347, and completed under the Defense Advanced Research Projects Agency Submarine Technology Program under Office of Naval Research Grant N00014-89-J-1342. The support and encouragement of E. P. Rood and G. Jones is greatly appreciated. The Graduate College of The University of Iowa and the National Center for Supercomputing Applications Academic Affiliates Program provided a large share of the computer funds.

## References

[1]Kerwin, J. E., "Marine Propellers," *Annual Review of Fluid Mechanics,* Vol. 18, 1986, pp. 367–403.

[2]Morris, P. J., "The Three-Dimensional Boundary Layer on a Rotating Helical Blade," *Journal of Fluid Mechanics,* Vol. 112, 1981, pp. 283–296.

[3]Groves, N. C., and Chang, M., "A Differential Prediction Method for Three-Dimensional Laminar and Turbulent Boundary Layers of Rotating Propeller Blades," *Proceedings of the 15th ONR Symposium on Naval Hydraulics,* National Academy Press, Washington, DC, 1984, pp. 429–444.

[4]Stern, F., Kim, H. T., Patel, V. C., and Chen, H. C., "A Viscous-Flow Approach to the Computation of Propeller-Hull Interaction," *Journal of Ship Research,* Vol. 32, No. 4, 1988, pp. 246–262.

[5]Stern, F., Kim, H. T., Patel, V. C., and Chen, H. C., "Computation of Viscous Flow Around Propeller-Shaft Configurations," *Journal of Ship Research,* Vol. 32, No. 4, 1988, pp. 263–284.

[6]Chen, H. C., and Patel, V. C., "Calculation of Trailing-Edge, Stern and Wake Flows by a Time-Marching Solution of the Partially-Parabolic Equations," Iowa Institute of Hydraulic Research, Univ. of Iowa, Iowa City, IA, IIHR Rept. 285, 1985.

[7]Schetz, J. A., Peletier, D., and Mallory, D. A., "Experimental and Numerical Investigation of a Propeller with Three-Dimensional Inflow," *Journal of Propulsion and Power,* Vol. 4, No. 4, 1988, pp. 341–349.

[8]Whitfield, D. L., Swafford, T. W., Janus, R. A., Mulac, R. A., and Belk, D. M., "Three-Dimensional Unsteady Euler Solutions for Profans and Counter-Rotating Profans in Transonic Flow," AIAA Paper 87-1197, 1987.

[9]Matsuo, Y., Arakawa, C., Saito, S., and Kobayashi, H., "Navier-Stokes Computaions for Flowfields of an Advanced Turboprop," AIAA Paper 88-3094, 1988.

[10]Srinivasan, G. R., "Tip Vortices of Isolated Wings and Helicopter Rotor Blades," JAI Associates, Inc., Mountain View, CA, TR 87-01, 1988.

[11]Rai, M. M., "Unsteady Three-Dimensional Navier-Stokes Simulations of Turbine Rotor-Stator Interaction," AIAA Paper 87-2058, 1987.

[12]Gupta, A. K., Lilley, D. G., and Syred, W., *Swirl Flows,* Abacus, Tunbridge Wells, England, 1984.

[13]Kim, H. T., "Computation of Viscous Flow Around a Propeller-Shaft Configuration with Infinite-Pitch Rectangular Blades," Ph.D. Thesis, Univ. of Iowa, Iowa City, IA, 1989.

[14]Patel, V. C., Chen, H. C., and Ju, S., "Ship Stern and Wake Flows: Solutions of the Fully-Elliptic Reynolds-Averaged Navier-Stokes Equations and Comparisons with Experiments," Iowa Institute of Hydraulic Research, Univ. of Iowa, Iowa City, IA, IIHR Rept. 323, 1988.

[15]Kerwin, J. E., and Lee, C. S., "Prediction of Steady and Unsteady Marine Propeller Performance by Numerical Lifting-Surface Theory," *Transactions of Society of Naval Architects and Marine Engineers,* Vol. 86, 1978, pp. 218–253.